CRYSTAL GROWTH & DESIGN

pubs.acs.org/crystal

Article

Spin Crossover Coordination Polymers with Pyridine-Like Modification through Selective Guest Molecules

Published as part of a Crystal Growth and Design virtual special issue on Molecular Magnets and Switchable Magnetic Materials

Li Sun, Mamadou Ndiaye, Nour El Islam Belmouri, Koen Robeyns, Aurelian Rotaru, Kamel Boukheddaden, and Yann Garcia*

Cite This: *Cryst. Growth Des.* 2022, 22, 7555−7563

Read Online

ACCESS | Metrics & More | Article Recommendations | Supporting Information

ABSTRACT: A porous 3D Fe^{II} coordination polymer made of 4,4′-bipyridine ligands (**bipy**) and $[N(CN)_2]^-$ (**dca**) organic bridges, $[Fe(bipy)_2dca]ClO_4{\cdot}CHCl_3{\cdot}CH_3OH$ (**1**·$CHCl_3$·CH_3OH), has been synthesized as single crystals, by a slow diffusion technique at room temperature. Single-crystal X-ray diffraction analysis has shown that the structure of **1**·$CHCl_3$·CH_3OH presents large volume values of porosity (1790 $Å^3$ per iron atom). It crystallizes in the orthorhombic $Cmc2_1$ space group but undergoes a phase transition to *Cmca* at 298 K, presumably due to solvent release. According to magnetic data, this material displays a gradual spin crossover behavior, along with a thermal hysteresis loop of 15 K around 190 K. However, when lattice solvent molecules are removed, the magnetic behavior changes drastically resulting in more gradual spin conversion or even silencing the spin crossover behavior of the as-synthesized complex (**1**·$CHCl_3$·CH_3OH), evidencing the influence of guest molecules on the magnetic properties by host−guest interactions. This property was confirmed by spatiotemporal optical microscopy studies, performed on several single crystals. The generation of a host lattice that interacts with exchangeable guest species in a switchable fashion has implications for the generation of previously undeveloped advanced materials with applications in areas such as molecular sensing.

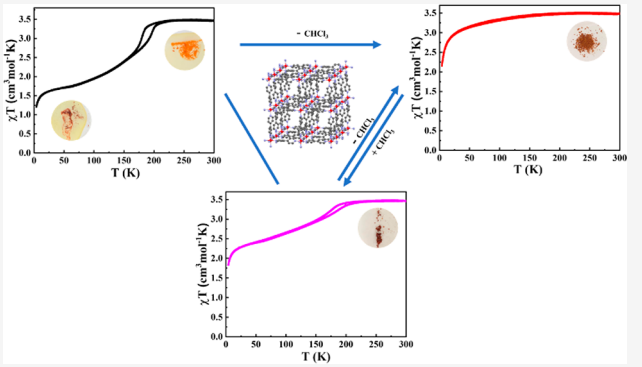

INTRODUCTION

So far, a large number of $3d^4$−$3d^7$ transition metal compounds display different spin state behaviors due to different electronic distribution states.[1−3] In particular, $3d^6$ Fe^{II} compounds are able to exhibit a spin crossover (SCO) between paramagnetic high-spin (HS, t_{2g}^4 e_g^2, $S = 2$) and diamagnetic low-spin (LS, t_{2g}^6 e_g^0, $S = 0$) states under external physical constraints such as temperature, pressure, and light irradiation.[4,5] In addition, guest molecules are known to present subtle effects on the SCO behavior of Fe^{II} compounds, accompanied by significant changes in macroscopic properties such as their magnetism or their color.[6−11] Therefore, Fe^{II} SCO compounds are recognized to have great potential applications in the development and application of high-technology devices based on sensing, information storage, molecular switching, display technology, optics, magnetism, etc.[12−14]

Dating back to the 1960s, the first mononuclear Fe^{II} SCO compound was successfully synthesized by Baker *et al.*[15] It was a grand milestone in the history of the development of SCO compounds, which was boosted by the discovery of Mössbauer spectroscopy, which was readily applied to these materials.[16] Since then, the increasing interest in the study of SCO compounds has led to a variety of Fe^{II} SCO compounds constructed with nitrogen-containing ligands being reported one after another. In particular, in 1993, Kahn *et al.*[17] successfully synthesized the first Fe^{II} SCO 1D coordination polymer (CP), switching at room temperature along with a memory effect, which opened the pathway to future applications. At the same time, the development of Fe^{II} SCO compounds has been pushed to an unprecedented climax, and a solid foundation has been laid for the development of Fe^{II} SCO CPs. In recent years, 2D/3D SCO CPs with outstanding performances have continuously received great attention and development.[18−20] 2D/3D SCO CPs with porosity provide a natural and excellent platform for the encapsulation and

Received: September 26, 2022
Revised: November 2, 2022
Published: November 20, 2022

https://doi.org/10.1021/acs.cgd.2c01081
Cryst. Growth Des. 2022, 22, 7555−7563

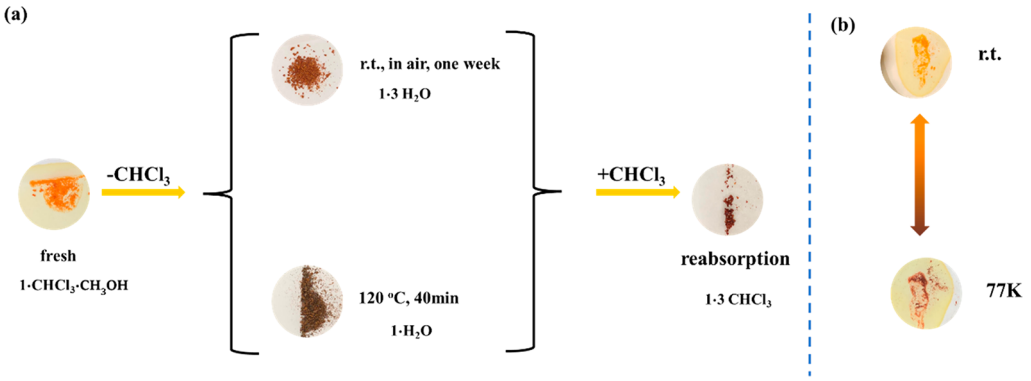

Figure 1. Color changes of (a) $1{\cdot}CHCl_3{\cdot}CH_3OH$, $1{\cdot}3H_2O$, and $1{\cdot}H_2O$ and reabsorption ($1{\cdot}3CHCl_3$) at room temperature (b) $1{\cdot}CHCl_3{\cdot}CH_3OH$ at 77 K and at room temperature.

locking of guest molecules,[21,22] which in turn modulates SCO through the interactions between host and guest molecules (such as van der Waals forces, hydrogen bonding interactions,[9,23,24] $\pi-\pi$ interactions,[25,26] structural rearrangement,[27] etc.). Such as in the SCO frameworks, $Fe^{II}(L^{N3})[M^{I}(CN)_2]_2{\cdot}$(Guest) (Guest = nitrobenzene, benzonitrile, *o*-dichlorobenzene; M^I = Ag, Au; L^{N3} = 1,3,5-tris(pyridin-4-ylethynyl)-benzene)[21] or in $[Fe(tpa)(NCX)_2]{\cdot}$guest; X = S, Se; guest = H_2O, CH_3OH, C_2H_5OH, *n*-PrOH and *i*-PrOH, CH_2Cl_2, $CHCl_3$, and CH_3CN, where magnetic properties are dramatically influenced by lattice guest solvent molecules.[6,28]

Among the many SCO Fe^{II} CPs, those with pyridine-like ligands are extremely favored.[29−34] Due to the aforementioned supramolecular forces between the guest molecules and the host lattice, these forces are able to change not only the coordination effect of the system but also the transition temperature[9,24] and the degree of spin conversion,[25] and even silence the SCO behavior.[35] For instance, the thermal hysteresis width was expanded up to 73 K by replacing the original solvents with naphthalene in the 1D channel of the SCO metal−organic framework, $[Fe(dpb)[Au(CN)_2]_2]{\cdot}n$Solv (dpb = 1,4-di(pyridin-4-yl)benzene; *n*Solv = 1.5DMF·0.3EtOH·0.2C_6H_{12}).[25] In another example, CPs maintain the HS state after solvent molecules escape.[36]

In this study, we report on the synthesis, crystal structures, and magnetic behavior of a novel 3D CP framework built from 4,4′-bipyridine (**bipy**) ligands and $[N(CN)_2]^-$ (**dca**) organic bridges and determined its guest-dependent SCO behavior (host−guest interaction) through introduction of $CHCl_3$ guest molecules in the cavities of the 3D framework. This is formulated as $[Fe(bipy)_2dca]ClO_4{\cdot}$Guest (**1**·Guest = $1{\cdot}CHCl_3{\cdot}CH_3OH$). Interestingly, the as-synthesized complex, $1{\cdot}CHCl_3{\cdot}CH_3OH$, has turned out to exhibit a remarkable SCO transformation process, accompanied by a color change, involving reversible exchange of small volatile molecules at room temperature (from orange to gold brown) and at low temperatures (from orange to dark brown, 77 K). The complex, $1{\cdot}CHCl_3{\cdot}CH_3OH$, undergoes SCO behavior with a thermal hysteresis loop of 15 K width around 190 K. These transformations are coupled to dramatic optical, magnetic, and crystallographic changes, thus converting this porous material into a robust low-temperature switch, sensitive to $CHCl_3$ molecules.

RESULTS AND DISCUSSION

Synthesis. Single crystals were grown by diffusing a solution of 4,4′-bipyridine (bipy) in chloroform layered on the bottom by a solution of $Fe(ClO_4)_2{\cdot}6H_2O$, Na(dca), ascorbic acid in methanol. NMR analysis indicates methanol and chloroform molecules are locked in the cavities of fresh crystals ($1{\cdot}CHCl_3{\cdot}CH_3OH$) in Figures S1 and S2. FT-IR confirmed the presence of noncoordinated ClO_4^- anions with a broad band at about 1069 cm^{-1} (Figure S3).[37] Thermogravimetric analysis recorded from room temperature up to 800 °C (Figure S4) showed a total weight loss from 25 to 160 °C of 18% (almost corresponding to the loss of one $CHCl_3$ molecule and CH_3OH molecules, 22%). The weight loss of guest molecules observed above 160 °C indicated a high stability temperature for this complex (Figure S4). The formula $[Fe(bipy)_2dca]ClO_4{\cdot}CHCl_3{\cdot}CH_3OH$ ($1{\cdot}CHCl_3{\cdot}CH_3OH$) was next confirmed by elemental analyses. When crystals of $1{\cdot}CHCl_3{\cdot}CH_3OH$ were left at room temperature in air for 1 week, a color change from orange to golden brown was observed leading to $1{\cdot}3H_2O$, as a consequence of the replacement of chloroform molecules by water molecules, from atmospheric humidity. When $1{\cdot}CHCl_3{\cdot}CH_3OH$ crystals were heated to 120 °C for 40 min, the color changed to dark brown, leading to $1{\cdot}H_2O$ (Figure 1a). Upon immersion of $1{\cdot}3H_2O$ in pure $CHCl_3$ (10 mL) for 1 week at room temperature, $1{\cdot}3CHCl_3$ was obtained as a crystalline solid which was collected by filtration. The same applies to $1{\cdot}H_2O$. More importantly, on cooling, the color of $1{\cdot}CHCl_3{\cdot}CH_3OH$ switches from orange to dark brown for $1{\cdot}CHCl_3{\cdot}CH_3OH$ at 77 K (Figure 1b), this effect being fully reversible and occurring in a few seconds (Movie S1). Therefore, these formulae ($1{\cdot}CHCl_3{\cdot}CH_3OH$, $1{\cdot}3H_2O$, $1{\cdot}H_2O$, and $1{\cdot}3CHCl_3$) were confirmed by elemental analysis, FT-IR, and TGA, as well as single crystal X-ray diffraction (which allowed us to determine the framework of $1{\cdot}CHCl_3{\cdot}CH_3OH$).

Single Crystal X-ray Structure Analysis. A single crystal of as-synthesized complex ($1{\cdot}CHCl_3{\cdot}CH_3OH$) was picked out from the mother liquor covered with paratone oil and flash cooled at 100 K, to prevent any solvent escape. Diffraction data were collected at 100 K, the temperature was subsequently increased by 4 K/min to 298 K, while keeping the crystal under N_2 atmosphere, and the same crystal was re-measured at 230 and 298 K. Crystal parameters correspond to the orthorhombic space groups $Cmc2_1$ (at 100 and 230 K) and *Cmca* at 298 K. Even at low temperature neither solvent molecules nor the ClO_4^- anions could be located in the pores,

https://doi.org/10.1021/acs.cgd.2c01081
Cryst. Growth Des. 2022, 22, 7555−7563

Table 1. Crystal Data and Structure Refinement Details for 1·$CHCl_3$·CH_3OH at 100, 230, and 298 K

Empirical formula	$C_{44}H_{32}Fe_2N_{14}$ [+ solvent]	$C_{44}H_{32}Fe_2N_{14}$ [+ solvent]	$C_{22}H_{16}FeN_7$ [+ solvent]
Formula weight	868.53	868.53	434.27
T (K)	100	230	298
Wavelength	0.71073 Å	0.71073 Å	0.71073 Å
Crystal system	Orthorhombic	Orthorhombic	Orthorhombic
Space group	$Cmc2_1$	$Cmc2_1$	$Cmca$
Unit cell dimensions	a = 17.0067(6) Å	a = 17.4483(6) Å	a = 17.594(7) Å
	b = 44.8358(12) Å	b = 45.899(2) Å	b = 23.303(6) Å
	c = 22.4272(7) Å	c = 22.9580(7) Å	c = 23.374(13) Å
V (Å)	17100.9(10)	18386.3(11)	9583(7)
Z	8	8	8
Density (calculated)	0.675 mg/m^3	0.628 g/cm^3	0.602 mg/m^3
Absorption coefficient	0.364 mm^{-1}	0.339 mm^{-1}	0.325 mm^{-1}
F(000)	3568	3568	1784
Crystal size	0.40 × 0.15 × 0.12 mm^3	0.44 × 0.44 × 0.15 mm^3	0.40 × 0.15 × 0.12 mm^3
Theta range for data collection	2.872−26.148°	2.498−26.606°	2.898−20.828°
Reflections collected	60483	38227	13585
Independent reflections	17513 [$R_{(int)}$ = 0.0584]	17724 [$R_{(int)}$ = 0.0504]	2569 [$R_{(int)}$ = 0.1095]
Completeness to θ_{max}	99.7%	99.6%	97.9%
Absorption correction	Semiempirical from equivalents		
Max and min transmission	1.00000 and 0.39385	1.00000 and 0.33518	1.00000 and 0.61609
Refinement method	Full-matrix least-squares on F^2		
Data/restraints/parameters	17513/868/621	17724/829/613	2569/138/146
Goodness-of-fit on F^2	1.095	1.115	1.079
Final R indices [I > 2sigma(I)]	R_1 = 0.0684, wR_2 = 0.1682	R_1 = 0.0740, wR_2 = 0.1788	R_1 = 0.1529, wR_2 = 0.3243
R indices (all data)	R_1 = 0.1134, wR_2 = 0.1918	R_1 = 0.1108, wR_2 = 0.2024	R_1 = 0.1937, wR_2= 0.3565
Largest diff. peak and hole	0.454 and −0.343 e.Å^{-3}	0.616 and −1.176 e.Å^{-3}	1.808 and −1.221 e.Å^{-3}

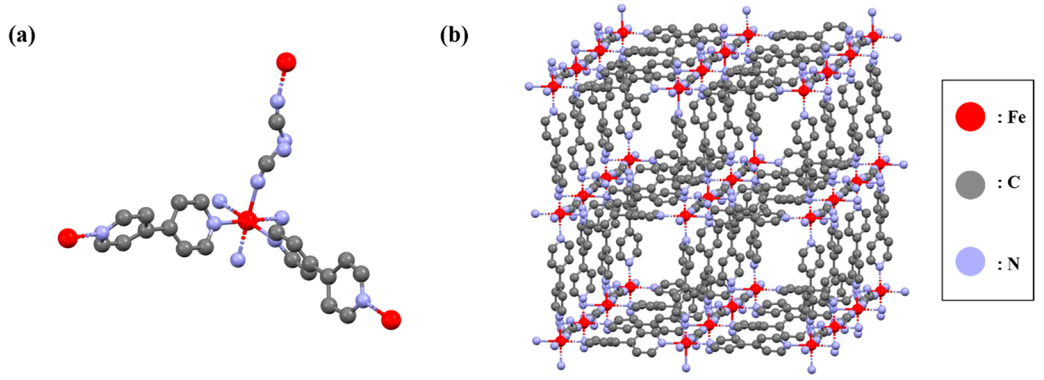

Figure 2. (a) A fragment of 1·$CHCl_3$·CH_3OH showing coordination environment (298 K). (b) View of one 3D network in 1·$CHCl_3$·CH_3OH without solvent molecules and ClO_4^- anions (298 K). All hydrogen atoms were omitted too for a sake of clarity.

despite the high-resolution data (0.81 Å). The disordered solvent contribution was treated with the squeeze algorithm in PLATON.[38] Crystallographic and refinement details for 1·$CHCl_3$·CH_3OH are shown in Table 1. As can be seen from the unit cell parameters, the temperature profile induces a phase transition going from a noncentrosymmetric $Cmc2_1$ unit cell with two independent Fe atoms (at 100 and 230 K) to the centrosymmetric space group $Cmca$, which is halved in volume at 298 K. Besides the expected thermal expansion, no phase transformation was observed up to 230 K (Table 1 and Table S2). In the room temperature structure, the rotational disorder of most pyridyl groups around the molecular axis, and to lesser extent the disorder of the **dca** linker, is relaxed, and all Fe atoms are crystallographically equal. All Fe^{II} atoms are in a distorted [$Fe^{II}N_6$] octahedral coordination environment at 298 K (Figure 2a), the four equatorial positions are occupied by **bipy** ligands, forming a layer, while the two axial positions are occupied by nitrogen atoms from the bridging **dca** anions linking those layers to form a 3D porous network framework (enclosing the solvent cavities taking up approximately 66% of the unit cell volume at 298 K) (Figure 2b). On cooling, a change in the Fe−N bond lengths and a unit cell contraction is observed, due to the molecular volume change between the HS and LS states (Table S1). At 100 K, the average Fe−N bond length is 2.051 Å in agreement with LS Fe^{II} ions and increases to reach 2.228 Å at 298 K, indicating HS Fe^{II} ions (Table S1). At 100 K, the average distance of $Fe^{II}\cdots Fe^{II}$ through the 4,4′-bipyridine ligands, within the layers is 11.215 Å (11.671 Å, 298 K) while the shortest $Fe^{II}\cdots Fe^{II}$ distance between adjacent layers, across the bridging **dca** anion, is 8.498 Å (8.797 Å, 298 K).

Powder X-ray Diffraction Analysis. An elegant way to study solvents effect on SCO behavior is to carry out the solvent exchange to obtain solvent-included compounds. From

https://doi.org/10.1021/acs.cgd.2c01081
Cryst. Growth Des. 2022, 22, 7555−7563

1·$CHCl_3$·CH_3OH, we noticed that the framework structure is thermally stable up to 160 °C (Figure S4) and that its SCO behavior could be modified through a desorption−absorption process (Figure 4 and Figure S8), accompanied by different colors (Figure 1). Therefore, it was anticipated that modification of the solvent content and nature may lead to different SCO behaviors. In fact, chloroform and methanol molecules of **1**·$CHCl_3$·CH_3OH can be exchanged with other solvent molecules by directly drying crystals at room temperature or by immersion in pure solvents. Powder X-ray diffraction (PXRD) of **1**·$CHCl_3$·CH_3OH, **1**·$3H_2O$, and **1**·$3CHCl_3$ are shown in Figure 3. The pattern obtained from **1**·

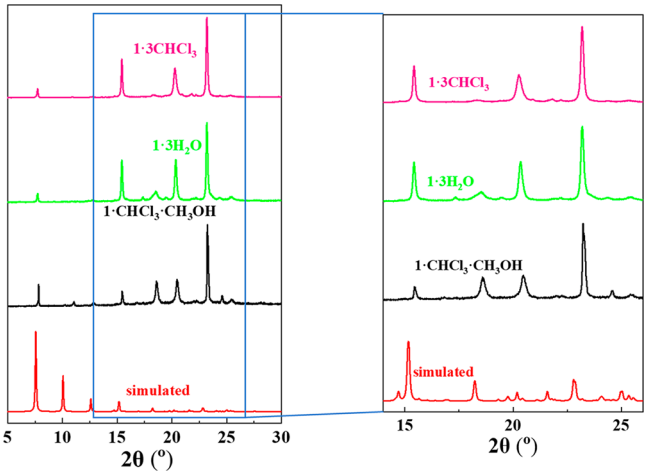

Figure 3. PRXD pattern of **1**·$CHCl_3$·CH_3OH along with the simulated one from single crystal X-ray diffraction for comparison (data recorded at 298 K), along with the ones of **1**·$3H_2O$ and **1**·$3CHCl_3$ at room temperature (Cu Kα radiation, λ = 1.5148 Å).

$CHCl_3$·CH_3OH is in fairly good agreement with the simulated single-crystal diffractogram, and nicely fits with the ones obtained for **1**·$3H_2O$ and **1**·$3CHCl_3$, thus indicating that the crystallinity and framework structure of the compounds remain intact after solvent exchange (desorption−reabsorption).

An interesting question concerns the determination of the transition temperature of the crystallographic phase transition, detected by single crystal X-ray diffraction from $Cmc2_1$ (100 K) to *Cmca* (298 K). To solve this issue, X-ray powder diffraction was carried out after filling a capillary with fresh single crystals of **1**·$CHCl_3$·CH_3OH. The batch was flash-cooled at 100 K and heated to 298 at 2 K/min. Every 5 or 10 K, the heating ramp was interrupted, allowing the crystal to stabilize and the unit cell parameters were subsequently determined (Table S2 and Figure S11). Besides the expected thermal expansion, no phase transformation was observed up to 230 K (Table 1, Table S2, and Figure S11). A noticeable increase in diffraction intensity was however observed from 160 K. Diffraction images were recorded at intermediate temperatures between the two already recorded, namely, at 230 and 290 K. No change in the space group was detected compared to the one recorded at 100 K ($Cmc2_1$). A full data collection was performed at 230 K showing a reduction of the disorder observed at 100 K (see Figure S12). The same unit cell was recorded upon further increasing the temperature up to 290 K (Table S2 and Figure S11), although with a reduction in diffraction quality starting around 270 K. Heating up to 298 K provoked the phase transformation, leading to the unit cell parameters reported for **1**·$CHCl_3$·CH_3OH at 298 K, but with a change of space group.

Magnetic Properties. The thermal dependence of χT (where χ is the molar magnetic susceptibility and T is temperature) for **1**·$CHCl_3$·CH_3OH, **1**·$3H_2O$, and **1**·H_2O was recorded at 2 K min^{-1} in the cooling and heating modes, respectively, over the range 300−4 K (Figure 4). For **1**·$CHCl_3$·

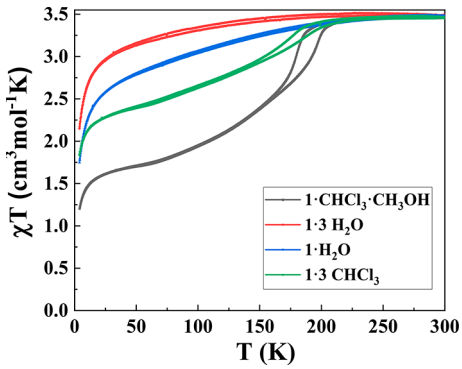

Figure 4. Plots of χT vs T for **1**·$CHCl_3$·CH_3OH, **1**·$3H_2O$ (dried 1 week, at r. t.), **1**·H_2O (heated at 393 K for 40 min), and **1**·$3CHCl_3$ (after reabsorption of $CHCl_3$).

CH_3OH χT = 3.48 cm^3 K mol^{-1} at 300 K, which fits well with HS Fe^{II} ions. As the temperature decreases, χT remains constant down to 220 K, after which it decreases rapidly at a transition temperature $T_{hy}^{\downarrow}$ = 180 K, defined at half of the hysteresis loop, on warming, by considering the first derivative $d(\chi T)/dT$ (Figure S9), and then smoothly down to 1.65 cm^3 K mol^{-1} at 33 K, indicating an incomplete transition (52% HS state). A third decrease is next observed below 20 K, as a result of the zero-field splitting of HS Fe(II) ions. On warming, similar behavior is observed delineating a hysteresis loop with $T_{hy}^{\uparrow}$ = 195 K (defined too at half of the hysteresis loop but on cooling, by considering the first derivative $d(\chi T)/dT$ (Figure S9)). A modified magnetic behavior is observed for the second cycle, with a transition that becomes more gradual and more incomplete (ca. 70% HS ions at 20 K), with $T_{hy}^{\downarrow}$ = 177 K and $T_{hy}^{\uparrow}$ = 187 K (Figure S8). This behavior most presumably originates from the release of some solvent molecules in the crystal lattice leading to the loss of host−guest interactions, which also leads to a change in the SCO behavior of the compound. This results in the increase of the HS molar fraction and leads to a more gradual SCO curve. Such a phenomenon leads to crystal defects which thereby increase the HS molar fraction and lead to a more gradual SCO curve. This hypothesis is confirmed when comparing magnetic data and single crystals X-ray diffraction data, which shows respectively a HS to LS switch, completed up to 52% and 85%, respectively. This difference is due to the care taken when recording single crystal X-ray diffraction data to prevent solvent evaporation, as stated above. A totally different behavior is observed for **1**·H_2O, which seems to be insensitive to temperature change (Figure 4), even after a second thermal cycle (Figure S8c). The same applies to **1**·$3H_2O$ which stabilizes the HS fraction more, thus showing the impact of solvent molecules on the spin state. The same behavior is found upon increasing the chloroform content, starting from **1**·$CHCl_3$·CH_3OH to **1**·$3CHCl_3$, with a ∼15 K downshift of the transition temperatures as well as a decrease by around 10 K of

https://doi.org/10.1021/acs.cgd.2c01081
Cryst. Growth Des. 2022, 22, 7555−7563

the hysteresis width ($T_{hy}^{\downarrow}$ = 178 K and $T_{hy}^{\uparrow}$ = 188 K (Figures S8d and S10).

Solvent molecules are known to have a remarkable effect on the crystal structures and magnetic properties of SCO compounds, given that intermolecular interactions involving such neutral species are known to influence SCO behavior.[10] In our complex, **1**·$CHCl_3$·CH_3OH, possibly, inclusion of solvent molecules through hydrogen bond (OH···O or OH···N) interactions is anticipated by methanol molecules in the crystal lattice. More importantly, the dispersion force could be dominant in the case of weak van der Waals interactions and Cl_3C−H···π or Cl_3C−H···Cl or Cl_3C−H···O or Cl_3C−H···N hydrogen bonding interaction between CH from $CHCl_3$ and **bipy**, $CHCl_3$, ClO_4^-, and **dca**, respectively.[39] Therefore, such a hydrogen bonding interaction could be responsible for the existence of a thermal hysteresis loop for the chloroform complexes.

Differential Scanning Calorimetry. Differential scanning calorimetry (DSC) was carried out on fresh crystals of **1**·$CHCl_3$·CH_3OH over the temperature range 113−298 K on warming/cooling at a scan rate of 2 K min^{-1}, to match that of magnetic measurements. The heat capacity temperature profile, $C_p(T)$ reveals on warming an endothermic peak at an onset temperature $T_o^{\uparrow}$ = 193 K and an exothermic peak on cooling at $T_o^{\downarrow}$ = 184 K (Figure 5). These peaks correspond to

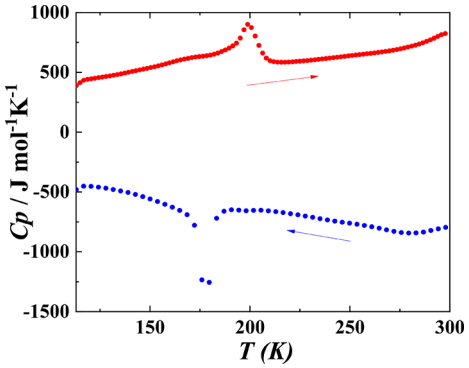

Figure 5. Heat capacity thermal profile on cooling and warming of **1**·$CHCl_3$·CH_3OH recorded at a scan rate of 2 K min^{-1}.

a first-order phase transition associated with the SCO behavior of **1**·$CHCl_3$·CH_3OH. The phase transition temperatures almost match the transition temperatures found by magnetic susceptibility measurements ($T_{hy}^{\downarrow}$ = 180 K and $T_{hy}^{\uparrow}$ = 195 K). The enthalpy associated with the SCO process was evaluated as ΔH = 4.59 kJ mol^{-1} and ΔS = 25.78 J mol^{-1} K^{-1}, considering the cooling process. Given that, in the case of quenched orbital moment, the electronic contribution to the entropy, $R\ln(5)$ = 13.33 J mol^{-1} K^{-1}, the vibrational (including intramolecular and phonons degrees of freedom) contribution to the SCO could be evaluated as ΔS_{vib} = 12.45 J mol^{-1} K^{-1}. These values are within the experimental range for Fe(II) SCO systems.[40−43]

Optical Properties. Cryogenic optical microscopy (OM) studies on a single crystal of **1**·$CHCl_3$·CH_3OH were performed in order to investigate the spatiotemporal features of the first-order transition more closely. The quantitative analysis of the OM data was performed by tracking the evolution of the transmitted light intensities of the RGB (Red, Blue, Green) pixel levels, from which the local and averaged optical densities were derived, which directly connect to the HS fraction of the material.[44,45] The results of the thermal-dependence of HS fraction, derived from OM, are summarized in Figure 6, where

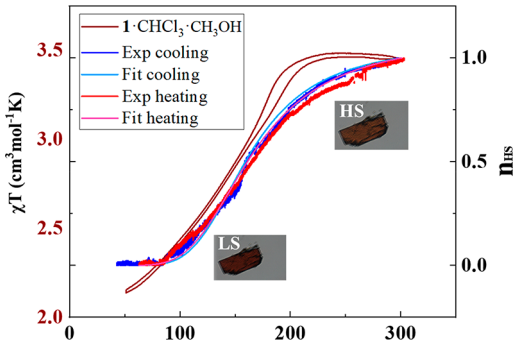

Figure 6. Thermal dependence of the averaged HS fraction (deduced from optical density) for a crystal of **1**·$CHCl_3$·CH_3OH on both cooling and warming modes, at 1 K min^{-1}. The fit derived from an Ising-like model is also shown along with the magnetic measurement after a second run for comparison, with ΔH = 6.23 kJ mol^{-1} and ΔS = 36 J mol^{-1} K^{-1}. Selected crystal images showing the spatiotemporal behavior of transmission images at characteristic temperatures 300 and 60 K in both HS and LS states are also inserted.

the SCO is found to proceed gradually over the range 100−300 K without any hysteresis effect (Figure 6). In the static snapshots, the colorimetric contrast between the HS and LS phases is obvious, accompanied by orange-red and deep-red colors in the HS and LS states, respectively. Corresponding real-time dynamics are provided in Movie S1 during the cooling process. The gradual type of transition is confirmed without the appearance of front interface features, even though striations (stripes) appear on the crystal surface during the transition, which are presumably due to lost host−guest interactions after the escape of guest solvent molecules. The comparison was done with the magnetic measurement during the second cycle (Figure S8a), which fits reasonably well, although in the case of SQUID measurements, an ensemble of crystals was recorded, while the OM signal corresponds to the response of one single crystal. Indeed, the magnetic signal results from the average responses of a large number of microcrystals (or microcrystalline powder) in which the particles have different sizes, shapes, and microstructures, while the OM are realized on unique single crystals. Magnetic measurements are then affected by several types of disorders on the parameters mentioned above, thus explaining the complex shape of the magnetic response which contains contributions of both gradual and first-order transitions with different transition temperatures. Due to the procedure of preparation of the sample in OM, it is difficult to avoid contact between the sample and air. Consequently, all studied single crystals have more or less absorbed water molecules, and contain less chloroform in their composition, which explains the discrepancy when comparing OM data with magnetic ones of **1**·$CHCl_3$·CH_3OH.

OM data were analyzed using an Ising model (see Experimental Section). A fair agreement is found in the following ranges of numerical parameters: Δ = 700−850 *K*, *J* = 5−10 K, and *g* ∼ 150−170, leading to the respective molar enthalpy and entropy changes ΔH ∼ 6.2−6.9 kJ mol^{-1} and ΔS ∼ 36.5−42 J $k^{-1}mol^{-1}$, which are close to the experimental values, considering the incomplete SCO behavior (Figure 4). Here, the interaction parameter *J* is very small compared to the

https://doi.org/10.1021/acs.cgd.2c01081
Cryst. Growth Des. 2022, 22, 7555−7563

ligand field energy Δ, resulting from the very gradual character of the transition, derived from OM observations.

On the other hand, the modeling of the magnetic data using the present model would require it to be extended in order to include at least two or several component samples, having different thermal evolutions: one with a gradual transition and another with a first-order transition. A more comprehensive approach would consist of considering a distribution of ligand fields and interaction parameters to reproduce the complex shape of the hysteretic magnetic response reported in Figure 6, which seems to include disorder effects in the structure, caused by the distributions of shapes and sizes of the studied crystals, as already noticed by OM. Lastly, the comparison between OM and magnetic data must be made with care owing to the difference of kinetic temperature (2 K/min for magnetic measurements and 1 K/min for OM) used in the two experiments.

CONCLUSIONS

Here we have reported on a Fe(II) spin crossover porous coordination polymer made of 4,4′-bipyridine ligands (**bipy**) and $[N(CN)_2]^-$ (**dca**) organic bridges, $[Fe(bipy)_2dca]ClO_4 \cdot CHCl_3 \cdot CH_3OH$ (**1**·$CHCl_3$·CH_3OH), whose magnetic investigation has shown a gradual one-step spin crossover well below room temperature and a thermal hysteresis loop in the higher temperature region, with a very noticeable color change (HS, orange; LS, dark brown). Calorimetric measurements on a fresh sample confirmed this behavior and indicated the occurrence of a first order phase transition, associated with the spin crossover behavior. On the other hand, temperature dependent optical microscopy measurements performed on unique single crystals (slowly exposed to air) revealed a spin crossover with uniform color change without front interface, indicating that the transition proceeds through a gradual and continuous change, which was found in fair agreement with the magnetic curve of the second cycle. The key of the reversible switch between the spin crossover behaviors reported in the magnetic measurement is attributed to the absence or presence of $CHCl_3$ molecules in the crystal cavities. Such a variety of magnetic behaviors illustrates that the degree of elastic frustration can be manipulated by molecular guests, which suggests that structural features that contribute to multistep switching may be subtler than previously anticipated.

EXPERIMENTAL SECTION

Materials and Characterization Methods. $Fe(ClO_4)_2 \cdot 6H_2O$, sodium dicyanamide (Na(dca)), and 4,4′-bipyridine (bipy) were purchased and used as received without further purification. Elemental analyses for C, H, and N were performed by Medac Ltd. (UK). NMR spectra were recorded on a Bruker AVANCE 500 MHz spectrometer. Chemical shifts (δ) are reported relative to the solvent residual peak (δ = 2.50, DMSO-d_6) for ^{1}H NMR. Fourier-transformed infrared (FT-IR) spectroscopy measurement was performed using an Equinox 55 (Bruker) equipped with an ATR modulus and an MCT detector. The Bruker software OPUS was used for data treatment (including ATR correction). Thermogravimetric analyses (TGA) were performed in $N_{2(g)}$ atmosphere (100 mL min^{-1}) at a heating rate of 5 °C min^{-1} from 25 to 800 °C using a Mettler Toledo TGA/SDTA 851e analyzer. DSC measurements were performed on a Mettler Toledo DSC with in $N_{2(g)}$ atmosphere at a heating rate of 2 K/min from 113 to 298 K. Powder X-ray diffraction (PXRD) patterns were collected on a D8-Advance diffractometer (Bruker, Germany) with Cu Kα radiation (λ = 1.5148 Å) operating at 40 kV and 30 mA. Magnetic susceptibilities were measured on a Quantum design MPMS-5s SQUID magnetometer. Magnetic data were corrected for the sample holder and diamagnetic contributions. The crystal sample was quickly loaded into a gelatin capsule and immediately inserted within the SQUID cavity.

Syntheses. *$[Fe(bipy)_2dca]ClO_4 \cdot CHCl_3 \cdot CH_3OH$ (**1**·$CHCl_3$·CH_3OH).* 4,4′-Bipyridine (16 mg, 0.1 mmol) was dissolved in chloroform (5 mL) (at bottom of a 15 mL tube) and layered below a filtered Fe^{II}:dca solution formed in an ascorbic acid solvent environment (to prevent Fe^{II} oxidation) from $Fe(ClO_4)_2 \cdot 6H_2O$ (36.2 mg, 0.1 mmol) and Na(dca) (9 mg, 0.1 mmol) in methanol (5 mL). The layer of the buffer solvent (containing V_{CHCl_3}:V_{MeOH} = 1:1, 2 mL) was placed between the layers before the top layer was added to prevent instant precipitation of powder. After a few days, orange crystals were formed at the layers interface. Yield ∼45% (29.4 mg). Elemental analysis (%) for $FeC_{24}H_{21}N_7Cl_4O_5$. Calcd: C 42.04, H 3.07, N 14.30; found: C 41.75, H 2.83, N 14.61.

*$[Fe(bipy)_2dca]ClO_4 \cdot 3H_2O$ (**1**·$3H_2O$).* Crystals of **1**·$CHCl_3$·CH_3OH were left at room temperature in air for 1 week. A color change from orange to golden brown was observed leading to **1**·$3H_2O$. Elemental analysis (%) for $FeC_{22}H_{22}N_7ClO_7$. Calcd: C 44.92, H 3.74, N 16.67; found: C 44.62, H 3.01, N 16.47.

*$[Fe(bipy)_2dca]ClO_4 \cdot H_2O$ (**1**·H_2O).* Crystals of **1**·$CHCl_3$·CH_3OH were heated to 120 °C for 40 min; the color changed to dark brown, leading to **1**·H_2O. Elemental analysis (%) for $FeC_{22}H_{18}N_7ClO_5$. Calcd: C 47.85, H 3.26, N 17.76; found: C 47.4, H 3.24, N 17.62.

*$[Fe(bipy)_2dca]ClO_4 \cdot 3CHCl_3$ (**1**·$3CHCl_3$).* Upon immersion of **1**·$3H_2O$ in pure $CHCl_3$(10 mL) for 1 week at room temperature, **1**·$3CHCl_3$ was obtained as a crystalline solid which was collected by filtration. Elemental analysis (%) for $FeC_{25}H_{19}N_7Cl_{10}O_4$. Calcd: C 33.62, H 2.13, N 10.98; found: C 33.60, H 2.43, N 11.66.

Crystallographic Data Collection and Structure Determination. Suitable crystals were selected for single-crystal X-ray diffraction analysis. X-ray intensity data for **1**·$CHCl_3$·CH_3OH were collected at 100 and 298 K on a MAR345 image plate using Mo Kα radiation (λ = 0.71073 Å). Data were integrated by CrysalisAlisPro (Agilent Technologies UK Ltd., Oxford, U.K., Xcalibur/Super Nova CCD system, CrysAlisPro Software system, versions 1.171.37.35) Absorption correction was applied using the integrated multiscan absorption algorithm. The structures were determined by direct methods (SHELXS) and refined by full-matrix least-squares on F^2 using SHELXL2014.[46] The location of the Fe atom was easily determined, and N and C atoms were subsequently located in the Fourier difference maps. The non-hydrogen atoms were refined anisotropically. The H atoms were introduced in calculated positions and refined with fixed geometry with respect to their carrier atoms. Disordered $CHCl_3$ and CH_3OH molecules could not be modeled properly. Thus, we have used the program SQUEEZE, a part of the PLATON package of crystallographic software, to calculate the solvent disorder area and move away their contributions to the overall intensity data.

Optical Microscopy. Optical microscopy measurements were carried out under a primary vacuum on single crystals (length × width = 166 μm × 66 μm) using a Nikon Eclipse LV100 microscope (objective ×20, numerical aperture 0.4), equipped with a closed cycle Oxford Instruments nitrogen-flow cryostat and connected to a digital camera Coreview Dalsa Falcon 1:4 M100 HG color, capable of capturing up to 100 frames per second. The OM images were recorded in transmission geometry using backward illumination by a tungsten halogen lamp, provided by the microscope. The sample was mounted in specific helium-tight cell designed for optical microscopy.[47] All measurements were performed using a temperature scan rate of 1 K min^{-1}. The camera was configured to save 5 images per second to record the spatiotemporal behavior of the spin transition. From every saved image, we can extract the optical density (OD), defined as

$$\mathrm{OD} = \log_{10}\left(\frac{I_{\mathrm{incident}}}{I_{\mathrm{transmitted}}}\right) \quad (1)$$

https://doi.org/10.1021/acs.cgd.2c01081
Cryst. Growth Des. 2022, 22, 7555−7563

where $I_{incident}$ corresponds to the bright field intensity while $I_{transmitted}$ corresponds to the intensity of the transmitted light through the single crystal. The OD which is the key parameter of the OM data analysis (recorded images) directly relates to the HS fraction, n_{HS}, of the single crystal, corresponding to the fraction of metal ions in the HS state, through the relation:[48]

$$n_{HS} = \frac{\langle OD(x, y)\rangle - OD_{LS}}{OD_{HS} - OD_{LS}} \quad (2)$$

where OD_{HS} and OD_{LS} are respectively the OD values in the HS and LS states and $\langle OD(x,y)\rangle$ is the spatially averaged optical density over the crystal at given temperature, T. In addition, each image of the experimental OM data was split into three OD components: red, green, and blue, depending on the single crystal thickness and color. From one compound to another, the signal quality (signal-to-noise ratio), would perhaps be better, in the red, green, or blue pixel. All the data are analyzed using Matlab programs developed by the Versailles group.

Modeling. The Ising model is used here to describe the SCO from the HS to the LS state by representing these states with fictitious spin states +1 and −1, respectively. The expression of the Hamiltonian of the system is given by[49]

$$H = -J\sum_{i,j} S_i S_j + \sum_i \Delta_{eff} S_i \quad (3)$$

where, $J > 0$ or $J < 0$ represent the ferroelastic or antiferroelastic interaction parameter between the SCO molecules. $\Delta_{eff} = (\Delta - k_B T \ln g)$ is the effective ligand field gap, which includes the quantity, Δ, corresponding to the difference of ligand fields between HS and LS states of isolated molecules and the entropic contribution, $k_B T \ln g$, resulting from the electronic and vibrational degeneracy ratio, $g = \frac{g_{HS}}{g_{LS}}$, between the HS and LS states. Using a mean-field treatment of Hamiltonian (eq 3), which follows very standard developments, we can obtain the following homogeneous free energy per site:

$$F_{hom} = \frac{1}{2}Jm^2 - k_B T \ln[2g\ \cosh(\beta(Jm - \Delta_{eff}))] \quad (4)$$

where $m = \langle S\rangle$ is the average fictitious magnetization per site and $\beta = \frac{1}{k_B T}$. The minimization of the analytical expression of the free energy, given in eq 4, with respect to the net "magnetization", m, by resolving the equation $\frac{\partial F_{hom}}{\partial m} = 0$, leads straightforwardly to the derived self-consistent eq 5:

$$m = \tanh[\beta(Jm - \Delta_{eff})] \quad (5)$$

The latter is connected to the HS fraction, n_{HS}, through the relation

$$n_{HS} = \frac{1 + \langle S\rangle}{2} = \frac{1 + m}{2} \quad (6)$$

The resolution of the self-consistent eq 5 gives the temperature dependence of the HS fraction, n_{HS}, which represents the fraction of molecules occupying the HS state stabilized at higher temperatures. The eq 5 admits a solution, $m = 0$, when $\Delta_{eff} = \Delta - k_B T \ln g = 0$. So, for $m = 0$, corresponding to $n_{HS} = \frac{1}{2}$, we derive the transition temperature of the system which cancels the effective field whose expression is written simply as $T_{eq} = \frac{\Delta}{k_B \ln g}$. It is interesting to note that the resolution of eq 5 does not need any numerical simulations to be performed; despite the self-consistent nature of this equation, it can be easily reversed by expressing the temperature as a function of the magnetization:

$$T = \frac{2(Jm - \Delta)}{k_B \ln\left[\left(\frac{1+m}{1-m}\right)\frac{1}{g}\right]} \quad (7)$$

then changing m from −1 to +1 by accounting for the limits gives, in a unique way, the associated temperature, T.

■ ASSOCIATED CONTENT

Supporting Information

The Supporting Information is available free of charge at https://pubs.acs.org/doi/10.1021/acs.cgd.2c01081.

Movie S1: Color change observed on **1**·$CHCl_3$·CH_3OH, when pouring a tube containing crystals to liquid nitrogen (MP4)

NMR, FT-IR, SQUID, TGA, DTA, and crystallographic information on **1**·$CHCl_3$·CH_3OH (PDF)

Accession Codes

CCDC 2209340−2209341 and 2214323 contain the supplementary crystallographic data for this paper. These data can be obtained free of charge via www.ccdc.cam.ac.uk/data_request/cif, or by emailing data_request@ccdc.cam.ac.uk, or by contacting The Cambridge Crystallographic Data Centre, 12 Union Road, Cambridge CB2 1EZ, UK; fax: +44 1223 336033.

■ AUTHOR INFORMATION

Corresponding Author

Yann Garcia − *Institute of Condensed Matter and Nanosciences, Molecular Chemistry, Materials and Catalysis (IMCN/MOST), Université catholique de Louvain, 1348 Louvain-la-Neuve, Belgium;* orcid.org/0000-0002-3105-0735; Email: yann.garcia@uclouvain.be

Authors

Li Sun − *Institute of Condensed Matter and Nanosciences, Molecular Chemistry, Materials and Catalysis (IMCN/MOST), Université catholique de Louvain, 1348 Louvain-la-Neuve, Belgium*

Mamadou Ndiaye − *Université Paris-Saclay, UVSQ, CNRS, GEMAC UMR 8635, F78035 Versailles, Cedex, France*

Nour El Islam Belmouri − *Université Paris-Saclay, UVSQ, CNRS, GEMAC UMR 8635, F78035 Versailles, Cedex, France*

Koen Robeyns − *Institute of Condensed Matter and Nanosciences, Molecular Chemistry, Materials and Catalysis (IMCN/MOST), Université catholique de Louvain, 1348 Louvain-la-Neuve, Belgium;* orcid.org/0000-0002-4763-4217

Aurelian Rotaru − *Department of Electrical Engineering and Computer Science and MANSiD Research Center, "Stefan cel Mare" University, Suceava 720229, Romania;* orcid.org/0000-0002-8782-7988

Kamel Boukheddaden − *Université Paris-Saclay, UVSQ, CNRS, GEMAC UMR 8635, F78035 Versailles, Cedex, France;* orcid.org/0000-0003-0464-1609

Complete contact information is available at: https://pubs.acs.org/10.1021/acs.cgd.2c01081

Notes

The authors declare no competing financial interest.

■ ACKNOWLEDGMENTS

This work was supported through the Fonds De La Recherche Scientifique—FNRS (PDR T.0095.21, CDR J.0168.22), the Université de Versailles-Paris Saclay, CNRS and Mol-CoSM ANR Project No. ANR-20-CE07-0028-01, the Ministère de l'Education et de la Recherche de Roumanie, and WBI. L. S. was supported by fellowship from the China Scholarship Council (201804910584).

DEDICATION

Dedicated to the memory of Prof. Dr. Philipp Gütlich who passed away on September 9, 2022, aged 88.

REFERENCES

(1) Hayami, S.; Komatsu, Y.; Shimizu, T.; Kamihata, H.; Lee, Y. H. Spin-crossover in cobalt(II) compounds containing terpyridine and its derivatives. *Coord. Chem. Rev.* **2011**, *255*, 1981−1990.

(2) Bertoni, R.; Lorenc, M.; Tissot, A.; Boillot, M. L.; Collet, E. Femtosecond photoswitching dynamics and microsecond thermal conversion driven by laser heating in Fe^{III} spin-crossover solids. *Coord. Chem. Rev.* **2015**, *282*−*283*, 66−76.

(3) Garcia, Y.; Gütlich, P. Thermal spin crossover in Mn(II), Mn(III), Cr(II) and Co(III) coordination compounds. *Top. Curr. Chem.* **2004**, *234*, 49−62.

(4) Breuning, E.; Ruben, M.; Lehn, J.-M.; Renz, F.; Garcia, Y.; Ksenofontov, V.; Gütlich, P.; Wegelius, E.; Rissanen, K. Spin crossover in a supramolecular Fe_4^{II} [2 × 2] grid triggered by temperature, pressure, and light. *Angew. Chem. Int. Ed* **2000**, *39*, 2504−2507.

(5) Murnaghan, K. D.; Carbonera, C.; Toupet, L.; Griffin, M.; Dirtu, M. M.; Desplanches, C.; Garcia, Y.; Collet, E.; Letard, J. F.; Morgan, G. G. Spin-state ordering on one sub-lattice of a mononuclear iron(III) spin crossover complex exhibiting LIESST and TIESST. *Chem.—Eur. J.* **2014**, *20*, 5613−5618.

(6) Sun, X.-P.; Wei, R.-J.; Yao, Z.-S.; Tao, J. Solvent Effects on the Structural Packing and Spin-Crossover Properties of a Mononuclear Iron(II) Complex. *Cryst. Growth Des* **2018**, *18*, 6853−6862.

(7) Neville, S. M.; Halder, G. J.; Chapman, K. W.; Duriska, M. B.; Moubaraki, B.; Murray, K. S.; Kepert, C. J. Guest tunable structure and spin crossover properties in a nanoporous coordination framework material. *J. Am. Chem. Soc.* **2009**, *131*, 12106−12108.

(8) Costa, J. S. n.; Jiménez, S. R.; Craig, G. A.; Barth, B.; Beavers, C. M.; Teat, S. J.; Aromí, G. Three-way crystal-to-crystal reversible transformation and controlled spin switching by a nonporous molecular material. *J. Am. Chem. Soc.* **2014**, *136*, 3869−3874.

(9) Pineiro-Lopez, L.; Valverde-Munoz, F. J.; Trzop, E.; Munoz, M. C.; Seredyuk, M.; Castells-Gil, J.; da Silva, I.; Marti-Gastaldo, C.; Collet, E.; Real, J. A. Guest induced reversible on-off switching of elastic frustration in a 3D spin crossover coordination polymer with room temperature hysteretic behaviour. *Chem. Sci.* **2021**, *12*, 1317−1326.

(10) Ni, Z.-P.; Liu, J.-L.; Hoque, M. N.; Liu, W.; Li, J.-Y.; Chen, Y.-C.; Tong, M.-L. Recent advances in guest effects on spin-crossover behavior in Hofmann-type metal-organic frameworks. *Coord. Chem. Rev.* **2017**, *335*, 28−43.

(11) Xue, J. P.; Hu, Y.; Zhao, B.; Liu, Z. K.; Xie, J.; Yao, Z. S.; Tao, J. A spin-crossover framework endowed with pore-adjustable behavior by slow structural dynamics. *Nat. Commun.* **2022**, *13*, 3510.

(12) Linares, J.; Codjovi, E.; Garcia, Y. Pressure and temperature spin crossover sensors with optical detection. *Sensors* **2012**, *12*, 4479−4492.

(13) Li, W.; Sun, L.; Liu, C.; Rotaru, A.; Robeyns, K.; Singleton, M. L.; Garcia, Y. Supramolecular $Fe(II)_4L_4$ cage for fast ammonia sensing. *J. Mater. Chem. C* **2022**, *10*, 9216−9221.

(14) Molnár, G.; Salmon, L.; Nicolazzi, W.; Terki, F.; Bousseksou, A. Emerging properties and applications of spin crossover nanomaterials. *J. Mater. Chem. C* **2014**, *2*, 1360−1366.

(15) Baker, W. A.; Bobonich, H. M. Magnetic properties of some high-spin Complexes of Iron(II). *Inorg. Chem.* **1964**, *3*, 1184−1188.

(16) Garcia, Y.; Gütlich, P. Chemical applications of Mössbauer spectroscopy, Mössbauer spectroscopy − Tutorial Book (Eds Y. Yoshida, G. Langouche). *Springer* **2013**, 23−89.

(17) Kröber, J.; Codjovi, E.; Kahn, O.; Grolière, F.; Jay, C. A spin transition system with a thermal hysteresis at room temperature. *J. Am. Chem. Soc.* **1993**, *115*, 9810−9811.

(18) Coronado, E.; Gimenez-Marques, M.; Minguez Espallargas, G.; Rey, F.; Vitorica-Yrezabal, I. J. Spin-crossover modification through selective CO_2 sorption. *J. Am. Chem. Soc.* **2013**, *135*, 15986−15989.

(19) Shin, J. W.; Jeong, A. R.; Jeoung, S.; Moon, H. R.; Komatsumaru, Y.; Hayami, S.; Moon, D.; Min, K. S. Three-dimensional iron(ii) porous coordination polymer exhibiting carbon dioxide-dependent spin crossover. *Chem. Commun.* **2018**, *54*, 4262−4265.

(20) Bartual-Murgui, C.; Akou, A.; Thibault, C.; Molnár, G.; Vieu, C.; Salmon, L.; Bousseksou, A. Spin-crossover metal−organic frameworks: promising materials for designing gas sensors. *J. Mater. Chem. C* **2015**, *3*, 1277−1285.

(21) Valverde-Munoz, F. J.; Munoz, M. C.; Ferrer, S.; Bartual-Murgui, C.; Real, J. A. Switchable spin-crossover hofmann-type 3D coordination polymers based on Tri- and Tetratopic ligands. *Inorg. Chem.* **2018**, *57*, 12195−12205.

(22) Garcia, Y.; Niel, V.; Muñoz, M. C.; Real, J. A. Spin crossover in 1D, 2D and 3D polymeric Fe(II) networks. *Top. Curr. Chem.* **2004**, *233*, 229−257.

(23) Liu, F.-L.; Tao, J. Hysteretic two-step spin-crossover behavior in two two-dimensional hofmann-type coordination polymers. *Chem.—Eur. J.* **2017**, *23*, 18252−18257.

(24) Jornet-Molla, V.; Gimenez-Saiz, C.; Canadillas-Delgado, L.; Yufit, D. S.; Howard, J. A. K.; Romero, F. M. Interplay between spin crossover and proton migration along short strong hydrogen bonds. *Chem. Sci.* **2021**, *12*, 1038−1053.

(25) Li, J.-Y.; He, C.-T.; Chen, Y.-C.; Zhang, Z.-M.; Liu, W.; Ni, Z.-P.; Tong, M.-L. Tunable cooperativity in a spin-crossover Hoffman-like metal−organic framework material by aromatic guests. *J. Mater. Chem. C* **2015**, *3*, 7830−7835.

(26) Meneses-Sánchez, M.; Piñeiro-López, L.; Delgado, T.; Bartual-Murgui, C.; Muñoz, M. C.; Chakraborty, P.; Real, J. A. Extrinsic vs. intrinsic luminescence and their interplay with spin crossover in 3D Hofmann-type coordination polymers. *J. Mater. Chem. C* **2020**, *8*, 1623−1633.

(27) Turo-Cortes, R.; Bartual-Murgui, C.; Castells-Gil, J.; Munoz, M. C.; Marti-Gastaldo, C.; Real, J. A. Reversible guest-induced gate-opening with multiplex spin crossover responses in two-dimensional Hofmann clathrates. *Chem. Sci.* **2020**, *11*, 11224−11234.

(28) Wei, R. J.; Tao, J.; Huang, R. B.; Zheng, L. S. Reversible and irreversible vapor-induced guest molecule exchange in spin-crossover compounds. *Inorg. Chem.* **2011**, *50*, 8553−8564.

(29) Halder, G. J.; Kepert, C. J.; Moubaraki, B.; Murray, K. S.; Cashion, J. D. Guest-dependent spin crossover in a nanoporous molecular framework material. *Science* **2002**, *298*, 1762−1765.

(30) Li, J. Y.; Yan, Z.; Ni, Z. P.; Zhang, Z. M.; Chen, Y. C.; Liu, W.; Tong, M. L. Guest-effected spin-crossover in a novel three-dimensional self-penetrating coordination polymer with permanent porosity. *Inorg. Chem.* **2014**, *53*, 4039−4046.

(31) Valverde-Munoz, F. J.; Bartual-Murgui, C.; Pineiro-Lopez, L.; Munoz, M. C.; Real, J. A. Influence of host-guest and host-host Interactions on the spin-crossover 3D Hofmann-type clathrates $\{Fe(II)(pina)[M(I)(CN)_2]_2\}$.xMeOH (M(I) = Ag, Au). *Inorg. Chem.* **2019**, *58*, 10038−10046.

(32) Orellana-Silla, A.; Valverde-Munoz, F. J.; Munoz, M. C.; Bartual-Murgui, C.; Ferrer, S.; Real, J. A. Halobenzene clathrates of the porous metal-organic spin-crossover framework $[Fe(tvp)_2(NCS)_2]_n$. Stabilization of a four-step transition. *Inorg. Chem.* **2022**, *61*, 4484−4493.

(33) Romero-Morcillo, T.; De la Pinta, N.; Callejo, L. M.; Pineiro-Lopez, L.; Munoz, M. C.; Madariaga, G.; Ferrer, S.; Breczewski, T.; Cortes, R.; Real, J. A. Nanoporosity, inclusion chemistry, and spin crossover in orthogonally interlocked two-dimensional metal-organic frameworks. *Chem.—Eur. J.* **2015**, *21*, 12112−12120.

(34) Real, J. A.; Andrés, E.; Muñoz, M. C.; Julve, M.; Granier, T.; Bousseksou, A.; Varret, F. Spin crossover in a catenane supramolecular system. *Science* **1995**, *268*, 265−267.

(35) Steinert, M.; Schneider, B.; Dechert, S.; Demeshko, S.; Meyer, F. A trinuclear defect-grid iron(II) spin crossover complex with a large

https://doi.org/10.1021/acs.cgd.2c01081
Cryst. Growth Des. 2022, 22, 7555−7563

hysteresis loop that is readily silenced by solvent vapor. *Angew. Chem. Int. Ed* **2014**, *53*, 6135−6139.
(36) Adams, C. J.; Munoz, M. C.; Waddington, R. E.; Real, J. A. Cooperative spin transition in the two-dimensional coordination polymer $[Fe(4,4'\text{-bipyridine})_2(NCX)_2].4CHCl_3$ (X = S, Se). *Inorg. Chem.* **2011**, *50*, 10633−10642.
(37) Zapata, F.; Garcia-Ruiz, C. The discrimination of 72 nitrate, chlorate and perchlorate salts using IR and Raman spectroscopy. *Spectrochim Acta A Mol. Biomol. Spectrosc* **2018**, *189*, 535−542.
(38) Spek, A. L. PLATON SQUEEZE: a tool for the calculation of the disordered solvent contribution to the calculated structure factors. *Acta Crystallogr. C Struct. Chem.* **2015**, *71*, 9−18.
(39) Allen, F. H.; Wood, P. A.; Galek, P. T. Role of chloroform and dichloromethane solvent molecules in crystal packing: an interaction propensity study. *Acta Crystallogr. B Struct. Sci. Cryst. Eng. Mater.* **2013**, *69*, 379−388.
(40) Sorai, M.; Seki, S. Phonon coupled cooperative low-spin $^1A_1$ high-spin $^5T_2$ transition in $[Fe(phen)_2(NCS)_2]$ and $[Fe(phen)_2(NCSe)_2]$ crystals. *J. Phys. Chem. Solids* **1974**, *35*, 555−570.
(41) Gütlich, P.; Garcia, Y.; Goodwin, H. A. Spin crossover phenomena in Fe(II) complexes. *Chem. Soc. Rev.* **2000**, *29*, 419−427.
(42) Dirtu, M. M.; Naik, A. D.; Rotaru, A.; Spinu, L.; Poelman, D.; Garcia, Y. Fe(II) spin transition materials including an amino-ester 1,2,4-Triazole derivative, operating at, below, and above room temperature. *Inorg. Chem.* **2016**, *55*, 4278−4295.
(43) Xue, S.; Guo, Y.; Rotaru, A.; Muller-Bunz, H.; Morgan, G. G.; Trzop, E.; Collet, E.; Olah, J.; Garcia, Y. Spin crossover behavior in a homologous series of iron(II) complexes based on functionalized bipyridyl ligands. *Inorg. Chem.* **2018**, *57*, 9880−9891.
(44) Fourati, H.; Boukheddaden, K. Experimental evidence for the elastic long-range character of the spin crossover transition in cooperative single crystals. *Phys. Rev. B* **2020**, *101*, 224101.
(45) Varret, F.; Chong, C.; Slimani, A.; Garrot, D.; Garcia, Y.; Naik, A. D. Real-time observation of spin-transitions by optical microscopy. *Spin-Crossover Materials: Properties and Applications* **2013**, 425−441.
(46) Sheldrick, G. M. A short history of SHELX. *Acta Crystallogr. Sect. A: Found. Crystallogr.* **2008**, *64*, 112−122.
(47) Chong, C.; Mishra, H.; Boukheddaden, K.; Denise, S. p.; Bouchez, G.; Collet, E.; Ameline, J. C.; Naik, A. D.; Garcia, Y.; Varret, F. Electronic and structural aspects of spin transitions observed by optical microscopy. The case of $[Fe(ptz)_6](BF_4)_2$. *J. Phys. Chem. B* **2010**, *114*, 1975−1984.
(48) Fourati, H.; Ndiaye, M.; Sy, M.; Triki, S.; Chastanet, G.; Pillet, S.; Boukheddaden, K. Light-induced thermal hysteresis and high-spin low-spin domain formation evidenced by optical microscopy in a spin-crossover single crystal. *Phys. Rev. B* **2022**, *105*, 174436.
(49) Boukheddaden, K.; Fourati, H.; Singh, Y.; Chastanet, G. Evidence of photo-thermal effects on the first-order thermo-induced spin transition of $[\{Fe(NCSe)(py)_2\}_2(m\text{-bpypz})]$ spin-crossover material. *Magnetochemistry* **2019**, *5*, 21.

https://doi.org/10.1021/acs.cgd.2c01081
Cryst. Growth Des. 2022, 22, 7555−7563